Assessment of using field-aligned currents to drive the Global Ionosphere Thermosphere Model: A case study for the 2013 St Patrick's Day geomagnetic storm

Qingyu Zhu[1], Gang Lu[1], Astrid Maute[1], Yue Deng[2], Brian Anderson[3]

[1]High Altitude Observatory, National Center of Atmospheric Research, Boulder, CO, USA

[2]Department of Physics, University of Texas at Arlington, Arlington, TX, USA

[3]John Hopkins University Applied Physics Laboratory, Laurel, MD, USA

Corresponding author: Qingyu Zhu (qingyu@ucar.edu)

Key points:

- AMPERE FAC data are used to drive GITM to study the ionospheric response to the 2013 St Patrick's Day geomagnetic storm
- FAC-driven GITM simulation captures the DMSP ion drifts reasonably well at high latitudes.
- FAC-driven GITM simulation also reproduces the overall low- and mid-latitude ionospheric response to the geomagnetic storm but quantitative differences do exist.

Abstract

In this study, field-aligned currents (FACs) obtained from the Active Magnetosphere and Planetary Electrodynamics Response Experiment (AMPERE) dataset have been used to specify high-latitude electric potential in the Global Ionosphere Thermosphere Model (GITM). The advantages and challenges of the FAC-driven simulation are investigated based on a series of numerical experiments and data-model comparisons for the 2013 St Patrick's Day geomagnetic storm. It is found that the cross-track ion drift measured by the Defense Meteorological Satellite Program (DMSP) satellites can be well reproduced in the FAC-driven simulation when the electron precipitation pattern obtained from Assimilative Mapping of Ionospheric Electrodynamics (AMIE) technique is used in GITM. It is also found that properly including the neutral wind dynamo is very important when using FACs to derive the high-latitude electric field. Without the neutral wind dynamo, the cross-polar-cap potential and hemispheric integrated Joule heating could be underestimated by more than 20%. Moreover, the FAC-driven simulation is able to well reproduce the ionospheric response to the geomagnetic storm in the American sector. However, the FAC-driven simulation yields relatively larger data-model discrepancies compared to the AMIE-driven GITM simulation. This may result from inaccurate Joule heating estimations in the FAC-driven simulation caused by the inconsistency between the FAC and electron precipitation patterns. This study indicates that the FAC-driven technique could be a useful tool for studying the coupled ionosphere and

thermosphere system provided that the FACs and electron precipitation patterns can be accurately specified.

Plain Language Summary

Earth's ionosphere can be significantly disturbed during geomagnetic storms which can induce adverse effects on the communication and navigation. To mitigate such adverse effects, it is critical to accurately predict the storm-time ionospheric response using numerical models, which largely depend on how well the high-latitude electrodynamical forcings are specified. Although empirical models reflecting the average patterns of the high-latitude forcings are convenient, they do not well capture their variabilities. High-latitude forcing patterns derived from the data assimilation technique have also been used, but experts are needed for data processing. Recently, since the realistic field-aligned current (FAC) data are available, new approaches have been developed using FACs to drive models. However, improvements along with more validations of the FAC-driven approaches are needed. In this study, we utilize realistic FAC data to drive the Global Ionosphere Thermosphere Model (GITM). The advantages and challenges of the FAC-driven simulation are investigated based on a series of numerical experiments and data-model comparisons during an intense geomagnetic storm. It is found that the FAC-driven technique could be a useful tool for studying the coupled ionosphere and thermosphere system as long as the FACs and electron precipitation patterns can be accurately specified.

1. Introduction

During geomagnetic storms, the Earth's ionosphere-thermosphere (I-T) system can be significantly disturbed. For example, a sudden southward turning of the interplanetary magnetic field (IMF) often triggers an eastward electric field that can penetrate toward to the equatorial region, reinforcing the dayside fountain effect and increasing the F-region electron density at low and middle latitudes (e.g., Fejer & Scherliess, 1997; Huang et al., 2005; Mannucci et al., 2005; Tsurutani et al., 2004). Meanwhile, high-latitude electric fields and electron precipitation can be intensified, generating tremendous amount of Joule heating at high latitudes (Deng et al., 2018; Richmond, 2021; Knipp et al, 2021). Such heating could modify the nominal thermospheric circulation and generate equatorward disturbance winds, pushing plasma upward along the magnetic field line and increasing the F-region electron density (e.g., Lin et al., 2005; Lu et al., 2008). However, the disturbance wind could generate a westward electric field on the dayside through the dynamo process, which can suppress the dayside fountain effect (Blanc & Richmond, 1980; Scherliess & Fejer, 1997). In addition, Joule heating can also change the thermospheric temperature, density and composition, which in turn affects the electron density though chemical processes (e.g., Burns et al., 1995; Cai et al., 2021; Fuller-Rowell et al., 1994). Moreover, impulsive Joule heating produces large-scale traveling atmospheric disturbances (TADs), which can induce oscillations of the ionospheric electron density (e.g., Lu et al., 2020; Zhang et al., 2019; Lyons et al, 2019; Sheng et al, 2021; Pham et al., 2022).

The processes mentioned above have been well simulated in the general circulation models (GCM) for the Earth's I-T system, and the specification of high-latitude electrodynamic forcings (i.e., high-latitude electric field and electron precipitation) has an important implication in GCM simulations. Typically, empirical models, which represent the climatological distribution of the high-latitude electrodynamic forcing under a given condition, are used in GCMs. However, empirical models often fail to capture the dynamic spatiotemporal variations of high-latitude electrodynamic forcings (Heelis & Maute, 2020), leading to significant data-model discrepancies. To achieve better model-data comparison, more realistic high-latitude electric potential and electron precipitation patterns obtained from the data assimilation techniques, such as the Assimilative Mapping Ionospheric Electrodynamics (AMIE) procedure (Richmond & Kamide, 1988), are needed in storm-time GCM simulations (e.g., Lu et al., 2014, 2020). Although AMIE is able to better capture the spatial and temporal variations of the high-latitude electric field and electron precipitation patterns than empirical models, it requires large efforts to gather and process data from different data sources (Lu, 2017). Hence, the AMIE patterns are only available for limited storm events. Recently, several studies have tried to calculate the high-latitude electric potential using global field-aligned currents (FACs) derived from the Active Magnetosphere and Planetary Electrodynamics Response Experiment (AMPERE) magnetic field perturbation dataset (Anderson et al., 2014) along with pre-defined auroral electron precipitation or ionospheric conductance patterns. Such a technique serves as a midway between empirical models and time-consuming data assimilations (such as AMIE) for specifying the high-latitude electric potential pattern. Built on the work done by Marsal et al. (2012), Maute et al. (2021) developed a new FAC-driven technique to deal with the asymmetric FACs in the National Center of Atmospheric Research Thermosphere-Ionosphere-Electrodynamics General Circulation model (NCAR-TIEGCM, Qian et al., 2014) to study ionospheric and thermospheric responses to the moderate 28-29 May 2010 storm. Although Maute et al. (2021) used the fitted FAC patterns based on the AMPERE raw magnetic perturbations using a method described by Shi et al. (2020), the FAC-driven technique can be readily applied to the AMPERE FAC data directly. Recently, Robinson et al. (2021) developed another technique to calculate the high-latitude electric potential using the AMPERE FAC data, along with the empirically derived ionospheric conductances based on FACs (Robinson et al. 2020). However, their solver did not produce self-consistent results since the input FACs are not identical to the output FACs (calculated from the electric potential and ionospheric conductance) especially on dusk side. More recently, Chartier et al. (2022) also used the AMPERE FAC to drive the SAMI3 model (Huba et al., 2008), in which the auroral electron precipitation is specified by an empirical model developed by Hardy et al. (1985). A moderate substorm was investigated in their study, and they found that the electron density structure in the polar cap was better reproduced in the FAC-driven SAMI3 simulation than in the simulation driven by the Weimer empirical potential model (Weimer, 2005). However, the high-latitude neutral wind dynamo was not taken into account in their study, which

may lead to the inconsistency between the simulated and measured ion drifts on dawn side shown in their study.

Although the FAC-driven technique is capable of improving high-latitude electric field specifications as well as data-model comparisons, a comprehensive assessment of the FAC-driven simulation is still much needed in order to better understand the advantages and challenges of this new technique, especially under more disturbed geophysical conditions. Firstly, it is not fully understood how well the high-latitude electric field can be reproduced by the FAC-driven simulation. Maute et al. (2021) and Robinson et al. (2021) did not provide direct comparisons for the measured and derived electric fields, and the data-model comparisons shown in Chartier et al. (2022) were only based on a few cases and did not address whether or not the FAC-driven simulation can capture the magnitude of the measured ion drift. Hence, a more quantitative comparisons between the simulated and measured high-latitude electric fields is needed to determine the validity of the FAC-driven simulation. Secondly, the importance of the neutral wind dynamo to the FAC-driven simulation remains unknown. Specifically, how the neutral wind dynamo affects the FAC-driven simulation in terms of high-latitude electric field and Joule heating dissipation is yet to be quantified. Finally, it is not well understood how well the FAC-driven simulation can replicate the ionospheric response to the geomagnetic storm at low and middle latitudes. For these reasons, this paper presents a comprehensive investigation of the ionospheric response to the 2013 St Patrick's Day geomagnetic storm to highlight both the advantages and challenges of the FAC-driven simulation using the Global Ionosphere Thermosphere Model (GITM, Ridley et al., 2006).

The remaining of the paper is organized as follows. Section 2 introduces GITM and its modeling setup, the AMPERE FAC dataset used in the simulation, and other ionospheric observations used for model-data comparison. The FAC-driven technique is modified from that developed by Maute et al. (2021) with some simplifications and improvements, which is described in Section 3. In Section 4, the outputs from the FAC-driven simulation are compared with the high-latitude ion drift measurements, low- and mid-latitude ground-based total electron content (TEC) measurements as well as with the outputs from the GITM simulation using the AMIE electric potential and electron precipitation patterns to assess the performance of the FAC-driven simulation during the 2013 St Patrick's Day geomagnetic storm.

2. Model and data

2.1 GITM

GITM is a three-dimensional general circulation model for the Earth's upper atmosphere (Ridley et al., 2006). The density, velocity and temperature of neutrals, ions and electron are self-consistently solved in GITM. GITM has flexible options for the grid size, and it relaxes the hydrostatic assumption to allow the propagation of acoustic waves (Deng et al., 2021 and references therein).

The ionospheric electrodynamo solver in GITM used in this study is adopted from the NCAR ionospheric electrodynamo model described in Maute & Richmond (2017). It solves for the global distribution of the ionospheric electric fields associated with the neutral wind dynamo, high-latitude forcing, as well as gravity and plasma pressure gradient forces in modified magnetic apex coordinates (Laundal & Richmond, 2017; Richmond, 1995). This study only focuses on the electric fields associated with the neutral wind and magnetospheric forcing. The coupling between the GITM and the NCAR ionospheric electrodynamo solver has been described in Zhu et al. (2019). In this study, the spatial resolution of GITM for all simulations is 5° in geographic longitude and 2.5° in geographic latitude and 1/3 scale height in altitude, with a model time step of 2 s. As for the ionospheric electrodynamo solver, the reference height is set at 110 km and the number of grid points in the magnetic local time (MLT) and magnetic latitude (MLAT) directions are 100 and 161, respectively. The grid spacing in MLT is even, which gives a 0.24-h separation in MLT. The grid spacing in MLAT is uneven and the separation in MLAT between two adjacent grid points is about 2-3° in the auroral zone and is less than 0.5° near the geomagnetic equator.

Four GITM simulations (Runs 1-4) are carried out in this study, which are distinguished by the way the high-latitude electrodynamic forcings are specified. A summary of those four GITM simulations can be found in Table 1. In Run 1, the electric potential and electron precipitation patterns from the AMIE procedure are used, and it is referred to as the AMIE-driven simulation. The data inputs to AMIE for this event include ground magnetic perturbations measured by 217 ground stations (among them 44 were in the SH), cross-track ion drift data measured by Defense Meteorological Satellite Program (DMSP) F15, F16, F17 and F18 satellites, total electron energy flux and average energy inferred from the Special Sensor of Ultraviolet Spectrographic Imager (SSUSI) onboard DMSP F16, F17 and F18 satellites, the line-of-sight ion drifts measured by Super Dual Auroral Radar Network (SuperDARN) high frequency radar network, along with the horizontal magnetic perturbations measured by the Iridium satellite constellation and provided by the AMPERE dataset (Anderson et al., 2014). The temporal resolution of the AMIE patterns is 5 min, with a spatial resolution of 0.67 h in MLT and 1.67° in MLAT.

Runs 2-4 are the FAC-driven simulations in which the high-latitude electric potential is calculated using the AMPERE FACs along with the different types of pre-defined electron precipitation patterns. Specifically, the AMIE and ASHLEY-A electron precipitation patterns are used in Runs 2 and 3, respectively. ASHLEY-A is the electron precipitation component of a recently developed empirical model, Auroral Spectrum and High-Latitude Electric field variabilitY (ASHLEY, Zhu et al., 2021), which is developed based on the in-situ electron precipitation measurements by the DMSP satellites. ASHLEY-A is parameterized according to the IMF strength and clock angle as well as the solar wind velocity and density. In Run 4, the empirical auroral conductance pattern derived from FACs is used (Robinson et al., 2020). To obtain the total electron energy flux and average energy in Run 4, we first calculate the

ionospheric conductance related to the auroral precipitation according to the AMPERE FAC distributions based on the relationship developed by Robinson et al. (2020). The total energy flux and average energy are then inversely determined based on the formulas in Robinson et al. (1987). Runs 2-4 are referred to as FAC-AMIE, FAC-ASHLEY and FAC-Robinson simulations, respectively. The purpose of Runs 2-4 is to assess how the different auroral precipitation patterns may affect the FAC-driven simulation results.

2.2 AMPERE FAC

The AMPERE FAC patterns are derived from the magnetic field perturbation measurements from 66 satellites of the Iridium Communication constellation (Anderson et al., 2014). Each satellite flies in a near-polar orbit at an orbital altitude of 780 km and with an orbital period of 104 min. The 66 Iridium satellites are distributed along 6 orbital planes equally spaced in local time. Each Iridium satellite carries a 3-axis vector fluxgate magnetometer that is able to sample the vector magnetic field either at a rate of 19.44 s (standard rate) or 2.16 s (high rate). The quantification and validation of the Iridium magnetometer data have been discussed in several studies (Waters et al., 2020 and references therein). The measured magnetic perturbation data within a 10-min time window are fitted with spherical cap harmonic basis functions to obtain a global distribution of the magnetic perturbations at high latitudes (Green et al., 2006; Waters et al., 2001). Currently, the fitting uses a longitude order of 5 and latitude order of 20 between 0 and 60° colatitude in Altitude Adjusted Corrected Geomagnetic (AACGM) Coordinates (Baker & Wing, 1989), meaning that the intrinsic spatial resolution of fitted magnetic perturbation data are 3° in latitude and 2.4 h in local time (Anderson et al., 2014). FACs are then calculated from the curl of the fitted horizontal magnetic perturbations. The AMPERE FACs are assumed to flow radially inward and outward of the ionosphere, which is a reasonable approximation at high latitudes. Hence, the term FAC used hereafter is referred to as the radial currents unless otherwise stated. The spatial resolution of the fitted FAC patterns is 1 h in MLT and 1° in MLAT and the temporal resolution can be up to 2 min (Anderson et al., 2014). In this study, the 10-min resolution AMPERE FAC data are utilized.

Since the ionospheric electrodynamo solver in GITM computes the global electric potential pattern at the reference height of 110 km, the FAC data obtained from the AMPERE database are also mapped from 780 km to 110 km. The AMPERE FACs are then interpolated to the grids of the ionospheric electrodynamo solver, where it is assumed that the differences between the modified magnetic apex coordinates and AACGM coordinates at high latitudes are negligible. As mentioned in Marsal et al. (2012), this assumption can lead to a maximum absolute difference of 0.3° in latitude and 0.5° in longitude in the polar cap, which is much smaller than the grid size of the ionospheric electrodynamo solver. Before the interpolation, the AMPERE FAC data are smoothed in both MLT and MLAT directions using a weighted sliding window to smooth out the small-scale FAC structures in order to prevent numerical discontinuities.

The window length is 3 hours (i.e., 3 grid points) in MLT and is 5° (i.e., 5 grid points) in MLAT and the weight is $2^{-|n-\frac{N+1}{2}|}$ ($1 \leq n \leq N$, N=3 or 5; N is the window width and n is the grid point position within the window).

2.3 Ionospheric datasets

The horizontal cross-track ion drifts from the DMSP F16, F17 and F18 satellites in the Northern Hemisphere (NH) are used for the model-data comparison. All three DMSP satellites fly in circular Sun-synchronous orbits at an altitude of ~840 km with an inclination of ~98.8°. The horizontal cross-track ion drift measurements are taken by the onboard Special Sensor for Ions, Electrons and Scintillation (SSIES), which measures the ion drift every 1 second, and only the data with quality flags 1 and 2 are used. For the polar crossing (MLAT>45° segments of the trajectory) with good-quality data, a baseline correction is applied to remove the background corotation. The corrected horizontal cross-track ion drift measurements are then smoothed with a 13-point (~100 km) sliding window.

The vertical total electron content (TEC) data estimated from the ground-based dual-frequency global navigation satellite system (GNSS) receivers in the American Sector are also used for the data-model comparison. To calculate the vertical TEC, the first step is to calculate the line-of-sight TEC (i.e., line-integrated ionospheric electron density) by analyzing the processed L1 and L2 pseudorange and phase data (Rideout and Coster, 2006). The subsequent step is to convert the slant TEC to the vertical TEC using a mapping function described in Rideout and Coster (2006) and Vierinen et al. (2016).

3. FAC-driven technique

If the FAC and ionospheric conductance are specified, the high-latitude electric potential (Φ^R) can be calculated from the current continuity equation:

$$p^c \frac{\partial}{\partial \phi_m}\left[\frac{\Sigma^{N/S}}{\cos\lambda_m}\frac{\partial \Phi^{RN/S}}{\partial \phi_m} + \Sigma^{N/S}\ \frac{\partial \Phi^{RN/S}}{\partial |\lambda_m|}\right] + p^c \frac{\partial}{\partial |\lambda_m|}\left[\Sigma^{N/S}\frac{\partial \Phi^{RN/S}}{\partial \phi_m} + \Sigma^{N/S}\cos\lambda_m\ \frac{\partial \Phi^{RN/S}}{\partial |\lambda_m|}\right] - (1-p^c)\,\sigma^R R\cos\lambda_m \Phi$$

Here, ϕ_m and λ_m represent the magnetic longitude and latitude in the modified apex coordinates, respectively, and R denotes the radius of the ionosphere base (i.e., 6371 km + 110 km = 6481 km). The Σ_{ij} ($i, j = \phi,\ \lambda$) terms are the integrated conductivities along a field line. The K^D_{mj} ($j = \phi,\ \lambda$) terms are the integrated neutral dynamo current integrated along a field line. The superscripts N and S represent the hemispheres (N: Northern Hemisphere; S: Southern Hemisphere). Details about Σ_{ij} and K^D_{mj} can be found in Richmond (1995). σ^R is the reference conductivity and p^c is a factor varying with λ_m. p^c is 0 equatorward of $|\lambda_m| = 40°$ and is 1 poleward of $|\lambda_m| = 45°$ and linearly changes from 0 to 1 from $|\lambda_m| = 40°$ to $|\lambda_m| = 45°$, which ensures Φ^R is zero equatorward of $|\lambda_m| = 40°$. J_{mr} is the FAC input. Eq. 1 is basically a simplification of Eqs. 2-4 in Maute et al. (2021) but it only aims to solving for the

high-latitude potential instead of the global potential.

To avoid unrealistic electric fields in the region where the modeled ionospheric conductance is low, the FAC density is set as zero where the hemispheric field-line integrated Pedersen conductivity is below 1.5 S. Moreover, to avoid numerical issues, the input FAC is corrected to ensure that the hemispherically integrated FAC is zero following the method used in Maute et al. (2021).

Once the high-latitude electric potential (Φ^R) is specified, the global electric potential (Φ) is solved according to the following equation which is originally from Richmond and Maute (2014):

$$p\frac{\partial}{\partial\phi_m}\left[\frac{\Sigma^T}{\cos\lambda_m}\frac{\partial\Phi}{\partial\phi_m}+\Sigma^T\ \frac{\partial\Phi}{\partial|\lambda_m|}\right]+p\frac{\partial}{\partial|\lambda_m|}\left[\Sigma^T\frac{\partial\Phi}{\partial\phi_m}+\Sigma^T\cos\lambda_m\ \frac{\partial\Phi}{\partial|\lambda_m|}\right]-(1-p)\sigma^R R\cos\lambda_m\Phi=pR\left[\frac{\partial K_{\mathrm{m}}^{\mathrm{DT}}}{\partial\phi_m}+\ \frac{\partial(K$$

Here $(\cdot)^T$ represents the sum of the corresponding parameters from different hemispheres. p is 1 equatorward of $|\lambda_m| = 50^\circ$ and is 0 poleward of $|\lambda_m| = 55^\circ$ and linearly changes from 1 to 0 from $|\lambda_m| = 50^\circ$ to $|\lambda_m| = 55^\circ$. Similar to the default procedure used in the TIEGCM, the Φ^R in the NH is used to calculate Φ at low and middle latitudes which is symmetric in the two hemispheres. After that, the Φ at high latitudes in the high latitudes of SH is replaced by the Φ^R in the SH.

4. Results and discussions

4.1 Geophysical conditions

The 2013 St Patrick's Day geomagnetic storm is classified as an intense geomagnetic storm triggered by an interplanetary coronal mass ejection (ICME) which arrived at the Earth's bow shock at around 6 UT on 03/17/2013. Figure 1 shows the geophysical conditions during this event, including the variations of the IMF B_y and B_z components along with the AE and Dst indices. Both the AE and Dst indices are from the AMIE outputs. The AE index is derived from 98 stations between ° and ° MLAT in both hemispheres, and the Dst index is similar to the SYM-H index but using the magnetometer data from 56 stations between -40° and 40° MLAT. The ICME sheath region passed the Earth's bow shock between 6 UT and 15:30 UT, during which the IMF underwent significant oscillations. The Dst index dropped to -120 nT around 12 UT and gradually recovered until the arrival of the magnetic cloud at 15:30 UT. The IMF Bz turned southward during the passage of the magnetic cloud and remained southward for about 6 hours. The Dst decreased again until reach its minimum of -140 nT around 20:30 UT. During the main phase (6:00-20:30 UT), AE underwent two strong intensifications around 7:30 UT and 16:30 UT, respectively, and the maximum AE value reached ~2800 nT.

4.2 Comparison with the DMSP ion drift measurements

The high-latitude ion drifts from the FAC-driven simulation are compared with

the DMSP cross-track ion drift measurements to determine whether the FAC-driven simulation can provide reasonable high-latitude electric fields. Figure 2 shows the data-model comparison along DMSP F16 polar crossings in the NH and SH after the onset of the geomagnetic storm (i.e., 6 UT on 03/17). The FAC-AMIE simulation (Run 2) results are exhibited in Figure 2. As shown in Figure 2, the FAC-AMIE simulation is able to well capture the overall high-latitude ion drifts measured by the DMSP F16 satellites but with some quantitative differences. For example, the FAC-AMIE simulation sometimes underestimates the magnitude of the ion drift. In addition, the ion drifts in the polar cap (at the middle of each plot) from the FAC-AMIE simulation display large variations for some polar crossings. Comparisons along the polar crossings of DMSP F17 and F18 satellites can be found in Supplement Figures S1 and S2, which are similar to those shown in Figure 2. Overall, the FAC-driven technique used in this study works well in a general sense if the electron precipitation is well specified, giving us more confidence to explore the low- and mid-latitude ionospheric response using the FAC-driven simulation.

4.3 Impact of neutral wind dynamo on high-latitude electric potential calculation

Before examining the low- and mid-latitude ionospheric response in detail, it is worthwhile to explore the potential impact of the neutral wind dynamo on the high-latitude electric potential calculation and Joule heating estimation. For that purpose, we carry out a controlled FAC-AMIE simulation in which the high-latitude neutral wind dynamo is turned off (i.e., the term in the square bracket on the right-hand side of Eq. 1 is set to zero). The cross-polar-cap potential (CPCP) and total Joule heating in the NH from these two FAC-AMIE simulations are compared and the results are shown in Figure 3. As one can see, both the CPCP and hemispheric integrated Joule heating are underestimated after the onset of the storm if the neutral wind dynamo is excluded from the high-latitude electric potential calculation. On average, the CPCP and Joule heating are underestimated by 21% and 26%, respectively, in the controlled FAC run after the onset of the storm (i.e., 6 UT on 03/17), indicating the importance of including the neutral wind dynamo when using FACs to calculate the high-latitude electric potential. As discussed in Lu et al. (1995), the FACs at the top of the ionosphere is the sum of FACs due to the ionospheric electric field and FACs due to the neutral wind, and the FACs due to the neutral wind are in opposite directions of FACs due to the ionospheric electric field. Therefore, the ionospheric electric field and thus the Joule heating can be underestimated if the FACs due to neutral winds is neglected.

4.4 Low- and mid-latitude ionospheric response

The data-model comparison shown in Section 4.1 illustrates that the FAC-driven simulation can reasonably reproduce the measured high-latitude electric fields. In this subsection, we further examine the ionospheric response to the geomagnetic storm at low and middle latitudes from the FAC-driven simulation. The ionospheric response to the main phase of the geomagnetic storm in the Amer-

ican sector is the primary focus owing to the best TEC observations available over that region. Figure 4 shows the storm-quiet differential TEC maps from the observation (top row) and from the AMIE-driven (middle row) and FAC-AMIE (bottom row) simulations at four selected UTs on 03/17. The observation and simulation outputs at the corresponding UTs on 03/16 are used as the quiet-time reference. It is also worth pointing out that the color scale range for the GITM simulation is half of that for the GNSS data. As discussed in Zhu et al. (2022), this is because GITM tends to underestimate TEC, which could be attributed to the lack of plasmaspheric contribution as well as inaccurate top boundary conditions (Ridley et al., 2006). Improving the representation of the electron density in GITM is scheduled for a future work.

As shown in the top row of Figure 4, the negative storm effect (as represented by a TEC reduction) occurs almost everywhere at low and middle latitudes except around 40°S and around 15°N at 14 UT. Then, the positive storm effect (i.e., a TEC enhancement) intensifies around 15°N and around 40°S at 16 UT while other regions still undergo the negative storm effect. At 18 UT, the positive storm effect occurs between 10°N and 40°N, around 10°S and southward of 40°S but the negative storm effect takes place northward of 40°N, around 5°N and around 25°S. At 20 UT, the positive storm effect takes over almost the entire American sector except for the region poleward of 40°N where a strong storm-time enhanced density (SED) plume is embedded in the region with the negative storm effect.

As shown in the bottom two rows of Figure 4, both the AMIE-driven (Run 1) and FAC-AMIE (Run2) simulations can well reproduce the salient features seen in the TEC observation described above although data-model discrepancies do exist. For example, both the AMIE-driven and FAC-AMIE simulations show that the positive storm effect around 15°N has a wider longitudinal spanning than the observation at 14 UT. In addition, both simulations also indicate the positive storm effect around 15°S at 16 UT which is inconsistent with the observation. Compared to the AMIE-driven simulation, the FAC-AMIE simulation results have somewhat larger model-data discrepancies. For example, the FAC-AMIE simulation does not capture the strong positive storm effect around 10°N and 90°W at 16 UT. In addition, the FAC-AMIE simulation shows that the negative storm phase around 5°N is stronger than that around 25°S at 18 UT, which is opposite to what are seen in the observation. Moreover, the negative storm effect northward of 40°N is not well reproduced in the FAC-AMIE simulation.

As discussed in Zhu et al. (2022), the ionospheric response to the 2013 St Patrick's Day geomagnetic storm in the American sector at the four UTs shown in Figure 4 are mainly attributed to the TADs launched at high latitudes. Therefore, the different amount of Joule heating deposited at high latitudes between the AMIE-driven and FAC-AMIE simulations may be responsible for the different ionospheric responses shown in Figure 4. To verify that, Figure 5 presents the distributions of the electric potential, total electron energy flux and height-integrated Joule heating from the AMIE-driven and FAC-AMIE simulations

at 12:30 UT on 03/17. Even though the same electron precipitation pattern is used, the distributions of the electric potential and height integrated Joule heating show significantly quantitative differences. This is also true for other UTs (supplement Movie S1). As a result, the generation, propagation and interaction of TADs in the FAC-AMIE simulation can be different from those in the AMIE-driven simulation. Consequently, the low- and mid-latitude ionospheric response is different between these two simulations.

Figure 6 compares the disturbance meridional winds from the AMIE-driven and FAC-AMIE simulations along 70°W to illustrate the differences in the TADs from those two simulations. It is clear that the generation, propagation and interaction of TADs are different between those two simulations, leading to different disturbance meridional winds at 5°N/25°S (i.e., ~15°/-15° MLAT). As discussed in Zhu et al. (2022), the negative storm effects at ±15° MLAT between 17 and 19 UT are mainly caused by the disturbance meridional winds associated with TADs and the magnitude of the negative storm effects depend on the magnitudes of disturbance meridional winds. Figure 7 compares the storm-quiet differences of the electron density and meridional wind at 5°N/25°S and at 70°W from the AMIE-driven and FAC-AMIE simulations. Comparing to the AMIE-driven simulation, the disturbance meridional winds between 16 and 19 UT are stronger/weaker at 5°N/25°S in the FAC-AMIE simulation, so that the negative storm effect at 18 UT intensifies/subsides at 5°N/25°S in the FAC-AMIE simulation. As a result, the negative storm effect in the NH is stronger than SH in the FAC-AMIE simulation at 18 UT, which is opposite to the AMIE-driven simulation result and the observation (Figure 4).

4.5 Impact of electron precipitation on the FAC-driven simulation

As described in Section 3, the FAC-driven technique calculates the high-latitude electric fields based on prescribed auroral electron precipitation patterns. Therefore, how the auroral precipitation pattern is specified will directly affect the derived high-altitude electric fields, which in turn affects the Joule heating estimation. Due to a lack of global auroral electron precipitation observations, it is very challenging to accurately specify the global electron precipitation pattern (and thus the auroral conductance pattern) at certain times, especially during geomagnetic storms. As a result, the auroral electron precipitation patterns used in the FAC-driven simulation are subject to large uncertainties. To evaluate how the different electron precipitation patterns may affect the FAC-driven simulation results, two additional FAC-driven simulations are conducted in which the ASHLEY-A (Run 3) and Robinson (Run 4) electron precipitation patterns are used, respectively.

Figure 8 shows the distributions of the electric potential, total electron energy flux and height-integrated Joule heating from the FAC-ASHLEY and FAC-Robinson simulations at 12:30 UT on 03/17. It is clear that the CPCPs in the NH and SH from the FAC-ASHLEY simulation are larger than those from other simulations, which is related to the weaker auroral electron precipitation. The hemispheric power (HP) of ASHLEY is about 50-60% of the HP from the

AMIE and Robinson electron precipitation patterns. The contours of the electric potential are also denser in the FAC-ASHLEY simulation, meaning that the electric field in the auroral zone is stronger than that from other simulations in general. As a result, the maximum of the height-integrated Joule heating and hemispheric-integrated Joule heating in each hemisphere are largest in the FAC-ASHLEY simulation. As for the FAC-Robinson simulation, although the Robinson electron pattern gives the highest HP in each hemisphere at 12:30 UT, the maximum localized total electron energy flux is smaller than that from the AMIE pattern in each hemisphere. The larger HP may be due to the fact that the electron precipitation occurs in a broader area in the Robinson electron precipitation pattern than in the AMIE electron precipitation on the day side. However, the CPCP from the FAC-Robinson simulation in each hemisphere is comparable with the CPCP from the FAC-AMIE simulation even though the AMIE and Robinson electron precipitations are quite different. The distribution of Joule heating from the FAC-Robinson simulations has some differences from the FAC-AMIE simulation and the hemispheric-integrated Joule heating from the FAC-Robinson simulation is about 20% and 10% higher than that from the FAC-AMIE simulation in the NH and SH, respectively.

Figure 9 compares the CPCP, auroral hemispheric power and hemispheric-integrated Joule heating in the NH from different simulations between 03/16 and 03/18. It is evident that the CPCP from the FAC-ASHLEY simulation is much larger (can exceed 100 kV) than that from other simulations. However, the larger CPCP in the FAC-ASHLEY simulation may be unrealistic, since the data coverage used to derive the AMIE electric potential pattern is relatively abundant in the NH for this event so that the AMIE CPCP is likely to be close to the truth. The large CPCP from the FAC-ASHLEY simulation may indicate that the electron precipitation is underestimated by ASHLEY-A. The Robinson electron precipitation pattern, by contrast, gives the highest HP in general especially before the onset of the storm (i.e., 6 UT on 03/17), so that the CPCP and Joule heating in the FAC-Robinson simulation is smaller than those from the AMIE-driven and FAC-AMIE simulations before the onset of the storm. However, the FAC-Robinson simulation generally captures the AMIE CPCP after the storm onset, and so does the FAC-AMIE simulation. The hemispheric-integrated Joule heating from the FAC-AMIE and FAC-Robinson simulation is generally consistent with that from the AMIE-driven simulation except between 16 and 20 UT where the values from the FAC-AMIE and FAC-Robinson simulations are ~30% smaller than that from the AMIE-driven simulation. The underestimation of Joule heating may imply the auroral electron precipitation is overestimated by the AMIE and Robinson electron precipitation patterns during this period. Clearly, Figures 8 and 9 demonstrate that the estimation of CPCP and Joule heating can be significantly impacted by the pre-defined electron precipitation pattern in the FAC-driven simulation.

5. Summary

In this study, we utilized the AMPERE FAC to drive GITM using a tech-

nique modified from Maute et al. (2021). The advantages and challenges of the FAC-driven simulation were investigated based on the simulation results for the intense 2013 St Patrick's Day geomagnetic storm. It is found that the high-latitude cross-track ion drift measured by the DMSP satellites can be reproduced reasonably well when AMIE electron precipitation pattern is used to specify high-latitude electron precipitation in GITM. This indicates that the FAC-driven technique used in this study can be a convenient and useful tool to obtain high-latitude electric fields in GCMs if the electron precipitation is well specified. The impact of including the neutral dynamo effect into FAC-driven technique on the high-latitude electric potential calculation as well as the Joule heating estimation is also examined. It is found that the CPCP and hemispheric Joule heating are underestimated by more than 20% if the neutral dynamo effect is not taken into account, indicating that including the neutral wind dynamo is important. Moreover, the ionospheric response to the geomagnetic storm at low and middle latitudes has been carefully examined in the FAC-driven simulation using the AMIE electron precipitation pattern. It is found that the observed low- and mid-latitude ionospheric response to the main phase of the 2013 St Patrick's Day geomagnetic storm in the American sector can be well reproduced. However, compared to the AMIE-driven GITM simulation, some salient features cannot be well reproduced in the FAC-driven simulation, which may be attributed to the inaccurate Joule heating estimation associated with the inaccuracies in the specification electron precipitation. In addition to the AMIE electron precipitation pattern, the ASHLEY-A and Robinson electron precipitation patterns are also used in the FAC-driven simulation. It is found that the high-latitude electric potential and Joule heating estimations can be significantly affected by the prescribed auroral electron precipitation pattern. This study demonstrates that the FAC-driven simulation could be a convenient and useful tool for the future global ionosphere and thermosphere simulation study. However, inaccurate prescribed auroral electron precipitation may limit the accuracy of FAC-driven simulation.

Acknowledgements

QZ was supported by the National Center for Atmospheric Research Advanced Study Program Postdoctoral Fellowship. GL was supported by in part by NASA under the Living with a Star (LWS) program under grant 80NSSC17K071 and the Heliophysics Supporting Research program under grant 80NSSC21K1673. QZ and GL were also supported by the NASA GOLD ICON Guest Investigators Program under grant 80NSSC22K0061 through the subaward 2021GC1619. AM was supported by NASA LWS under grant 80NSSC20K1784. GL and AM were also supported by AFOSR through award FA9559-17-1-0248. YD was supported by AFOSR through awards FA9559-16-1-0364 and NASA through grants 80NSSC20K0195, 80NSSC20K1786 and 80NSSC20K0606. This material is based upon work supported by the National Center for Atmospheric Research, which is a major facility sponsored by the National Science Foundation under Cooperative Agreement No. 1852977. We thank the support from the ISSI for the international team on "Multi-Scale Magnetosphere-Ionosphere-

Thermosphere Interaction". We would like to acknowledge high-performance computing support from Cheyenne (doi:10.5065/D6RX99HX) provided by National Center for Atmospheric Research's Computational and Information Systems Laboratory, sponsored by the National Science Foundation.

Open Research

We acknowledge use of NASA/GSFC's Space Physics Data Facility's OMNIWeb (or CDAWeb or ftp) service, and OMNI data. The OMNI data can be found at https://omniweb.gsfc.nasa.gov. The GNSS TEC and DMSP SSIES data are available at http://cedar.openmadrigal.org/. We thank the AMPERE team and the AMPERE Science Center for providing the Iridium-derived data products, which are available under http://ampere.jhuapl.edu/. The DMSP ion drift data are available at http://cedar.openmadrigal.org/index.html/. The AMIE outputs and AMIE-driven simulation results are stored at https://doi.org/10.5065/asf8-3d59. The FAC-driven simulation outputs are stored at: https://doi.org/10.5065/meak-p360.

References

Anderson, B. J., Korth, H., Waters, C. L., Green, D. L., Merkin, V. G., Barnes, R. J., & Dyrud, L. P. (2014). Development of large-scale Birkeland currents determined from the Active Magnetosphere and Planetary Electrodynamics Response Experiment. Geophysical Research Letters, 41(9), 3017–3025. https://doi.org/10.1002/2014GL059941

Baker, K. B., & Wing, S. (1989). A new magnetic coordinate system for conjugate studies at high latitudes. Journal of Geophysical Research: Space Physics, 94(A7), 9139–9143. https://doi.org/10.1029/JA094iA07p09139

Blanc, M., & Richmond, A. D. (1980). The ionospheric disturbance dynamo. *Journal of Geophysical Research: Space Physics*, *85*(A4), 1669–1686. https://doi.org/10.1029/JA085iA04p01669

Burns, A. G., Killeen, T. L., Deng, W., Carignan, G. R., & Roble, R. G. (1995). Geomagnetic storm effects in the low- to middle-latitude upper thermosphere. *Journal of Geophysical Research: Space Physics*, *100*(A8), 14673–14691. https://doi.org/10.1029/94JA03232

Cai, X., Burns, A. G., Wang, W., Qian, L., Solomon, S. C., Eastes, R. W., McClintock, W. E., & Laskar, F. I. (2021). Investigation of a Neutral "Tongue" Observed by GOLD During the Geomagnetic Storm on May 11, 2019. *Journal of Geophysical Research: Space Physics*, *126*(6), e2020JA028817. https://doi.org/10.1029/2020JA028817

Chartier, A. T., Huba, J. D., Sitaram, D. P., Merkin, V. G., Anderson, B. J., & Vines, S. K. (2022). High-Latitude Electrodynamics Specified in SAMI3 Using AMPERE Field-Aligned Currents. Space Weather, 20(1), e2021SW002890. https://doi.org/10.1029/2021SW002890

Deng Y., C. Lin, Q. Zhu & C. Sheng (2021), Influence of non-hydrostatic processes on the ionosphere-thermosphere, in *Space Physics and Aeronomy Collection Volume 4: Upper Atmosphere Dynamics and Energetics*, *Geophys. Monogr. Ser.*, vol. 261, edited by W. Wang and Y. Zhang, DOI: 10.1002/9781119507512.ch4, Chapt 4, AGU, Washington, D.C.

Fejer, B. G., & Scherliess, L. (1997). Empirical models of storm time equatorial zonal electric fields. *Journal of Geophysical Research: Space Physics*, *102*(A11), 24047–24056. https://doi.org/10.1029/97JA02164

Fuller-Rowell, T. J., & Evans, D. S. (1987). Height-integrated Pedersen and Hall conductivity patterns inferred from the TIROS-NOAA satellite data. Journal of Geophysical Research: Space Physics, 92(A7), 7606–7618. https://doi.org/10.1029/JA092iA07p07606

Fuller-Rowell, T. J., Codrescu, M. V., Moffett, R. J., & Quegan, S. (1994). Response of the thermosphere and ionosphere to geomagnetic storms. *Journal of Geophysical Research: Space Physics*, *99*(A3), 3893–3914. https://doi.org/10.1029/93JA02015

Green, D. L., Waters, C. L., Anderson, B. J., Korth, H., & Barnes, R. J. (2006). Comparison of large-scale Birkeland currents determined from Iridium and SuperDARN data. Annales Geophysicae, 24(3), 941–959. https://doi.org/10.5194/angeo-24-941-2006

Hardy, D. A., Gussenhoven, M. S., & Holeman, E. (1985). A statistical model of auroral electron precipitation. Journal of Geophysical Research: Space Physics, 90(A5), 4229–4248. https://doi.org/10.1029/JA090iA05p04229

Heelis, R. A., & Maute, A. (2020). Challenges to Understanding the Earth's Ionosphere and Thermosphere. *Journal of Geophysical Research: Space Physics*, *125*(7), e2019JA027497. https://doi.org/10.1029/2019JA027497

Huang, C.-S., Foster, J. C., & Kelley, M. C. (2005). Long-duration penetration of the interplanetary electric field to the low-latitude ionosphere during the main phase of magnetic storms. *Journal of Geophysical Research: Space Physics*, *110*(A11). https://doi.org/10.1029/2005JA011202

Huba, J. D., Joyce, G., & Krall, J. (2008). Three-dimensional equatorial spread F modeling. Geophysical Research Letters, 35(10). https://doi.org/10.1029/2008GL033509

Knipp, D., Kilcommons, L., Hairston, M., & Coley, W. R. (2021). Hemispheric asymmetries in Poynting flux derived from DMSP spacecraft. *Geophysical Research Letters*, 48, e2021GL094781. https://doi.org/10.1029/2021GL094781

Laundal, K. M., & Richmond, A. D. (2017). Magnetic coordinate systems. Space Science Reviews, 206(1–4), 27–59.

Lin, C. H., Richmond, A. D., Heelis, R. A., Bailey, G. J., Lu, G., Liu, J. Y., Yeh, H. C., & Su, S.-Y. (2005). Theoretical study of the low- and midlatitude ionospheric electron density enhancement during the October 2003 superstorm: Rel-

ative importance of the neutral wind and the electric field. *Journal of Geophysical Research: Space Physics*, *110*(A12). https://doi.org/10.1029/2005JA011304

Lu, G., Richmond, A. D., Emery, B. A., & Roble, R. G. (1995). Magnetosphere-ionosphere-thermosphere coupling: Effect of neutral winds on energy transfer and field-aligned current. *Journal of Geophysical Research: Space Physics*, *100*(A10), 19643–19659. https://doi.org/10.1029/95JA00766

Lu, G., Hagan, M. E., Häusler, K., Doornbos, E., Bruinsma, S., Anderson, B. J., & Korth, H. (2014). Global ionospheric and thermospheric response to the 5 April 2010 geomagnetic storm: An integrated data-model investigation. *Journal of Geophysical Research: Space Physics*, *119*(12), 10,358-10,375. https://doi.org/10.1002/2014JA020555

Lu, G., Zakharenkova, I., Cherniak, I., & Dang, T. (2020). Large-Scale Ionospheric Disturbances During the 17 March 2015 Storm: A Model-Data Comparative Study. *Journal of Geophysical Research: Space Physics*, *125*(5), e2019JA027726. https://doi.org/10.1029/2019JA027726

Lyons, L. R., Nishimura, Y., Zhang, S. R., Coster, A. J., Bhatt, A., Kendall, E., & Deng, Y. (2019). Identification of auroral zone activity driving large-scale traveling ionospheric disturbances. *Journal of Geophysical Research: Space Physics*, **124**, 700–714. https://doi.org/10.1029/2018JA025980

Mannucci, A. J., Tsurutani, B. T., Iijima, B. A., Komjathy, A., Saito, A., Gonzalez, W. D., Guarnieri, F. L., Kozyra, J. U., & Skoug, R. (2005). Dayside global ionospheric response to the major interplanetary events of October 29–30, 2003 "Halloween Storms." *Geophysical Research Letters*, *32*(12). https://doi.org/10.1029/2004GL021467

Marsal, S., Richmond, A. D., Maute, A., & Anderson, B. J. (2012). Forcing the TIEGCM model with Birkeland currents from the Active Magnetosphere and Planetary Electrodynamics Response Experiment. Journal of Geophysical Research: Space Physics, 117(A6). https://doi.org/10.1029/2011JA017416

Maute, A., & Richmond, A. D. (2017). F-Region Dynamo Simulations at Low and Mid-Latitude. Space Science Reviews, 206(1–4), 471–493. https://doi.org/10.1007/s11214-016-0262-3

Maute, A., Richmond, A. D., Lu, G., Knipp, D. J., Shi, Y., & Anderson, B. (2021). Magnetosphere-Ionosphere Coupling via Prescribed Field-Aligned Current Simulated by the TIEGCM. Journal of Geophysical Research: Space Physics, 126(1), e2020JA028665. https://doi.org/10.1029/2020JA028665

Newell, P. T., Sotirelis, T., & Wing, S. (2009). Diffuse, monoenergetic, and broadband aurora: The global precipitation budget. Journal of Geophysical Research: Space Physics, 114(A9). https://doi.org/10.1029/2009JA014326

Pham, K. H., Zhang, B., Sorathia, K., Dang, T., Wang, W., Merkin, V., Liu, H., Lin, D., Wiltberger, M., Lei, J., Bao, S., Garretson, J., Toffoletto, F., Michael, A., & Lyon, J. (2022). Thermospheric Density Perturbations

Produced by Traveling Atmospheric Disturbances During August 2005 Storm. *Journal of Geophysical Research: Space Physics, 127(2)*, e2021JA030071. https://doi.org/10.1029/2021JA030071

Qian, L., Burns, A. G., Emery, B. A., Foster, B., Lu, G., Maute, A., Richmond, A. D., Roble, R. G., Solomon, S. C., & Wang, W. (2014). The NCAR TIE-GCM: A Community Model of the Coupled Thermosphere/Ionosphere System. In J. Huba, R. Schunk, & G. Khazanov (Eds.), Geophysical Monograph Series (pp. 73–83). John Wiley & Sons, Ltd. https://doi.org/10.1002/9781118704417.ch7

Richmond, A. D. (1995). Ionospheric Electrodynamics Using Magnetic Apex Coordinates. Journal of Geomagnetism and Geoelectricity, 47(2), 191–212. https://doi.org/10.5636/jgg.47.191

Richmond, A. D., & Kamide, Y. (1988). Mapping electrodynamic features of the high-latitude ionosphere from localized observations: Technique. Journal of Geophysical Research: Space Physics, 93(A6), 5741–5759. https://doi.org/10.1029/JA093iA06p05741

Richmond, A. D., & Maute, A. (2014). Ionospheric Electrodynamics Modeling. In J. Huba, R. Schunk, & G. Khazanov (Eds.), Geophysical Monograph Series (pp. 57–71). John Wiley & Sons, Ltd. https://doi.org/10.1002/9781118704417.ch6

Richmond, A.D. (2021). Joule Heating in the Thermosphere. In Upper Atmosphere Dynamics and Energetics (eds W. Wang, Y. Zhang and L.J. Paxton). https://doi.org/10.1002/9781119815631.ch1

Rideout, W., & Coster, A. (2006). Automated GPS processing for global total electron content data. *GPS Solutions*, *10*(3), 219–228. https://doi.org/10.1007/s10291-006-0029-5

Ridley, A. J., Deng, Y., & Tóth, G. (2006). The global ionosphere–thermosphere model. Journal of Atmospheric and Solar-Terrestrial Physics, 68(8), 839–864. https://doi.org/10.1016/j.jastp.2006.01.008

Robinson, R. M., Kaeppler, S. R., Zanetti, L., Anderson, B., Vines, S. K., Korth, H., & Fitzmaurice, A. (2020). Statistical Relations Between Auroral Electrical Conductances and Field-Aligned Currents at High Latitudes. Journal of Geophysical Research: Space Physics, 125(7), e2020JA028008. https://doi.org/10.1029/2020JA028008

Robinson, R. M., Vondrak, R. R., Miller, K., Dabbs, T., & Hardy, D. (1987). On calculating ionospheric conductances from the flux and energy of precipitating electrons. Journal of Geophysical Research: Space Physics, 92(A3), 2565–2569. https://doi.org/10.1029/JA092iA03p02565

Robinson, R. M., Zanetti, L., Anderson, B., Vines, S., & Gjerloev, J. (2021). Determination of Auroral Electrodynamic Parameters from AMPERE Field-Aligned Current Measurements. Space Weather, 19(4), e2020SW002677. https://doi.org/10.1029/2020SW002677

Scherliess, L., & Fejer, B. G. (1997). Storm time dependence of equatorial disturbance dynamo zonal electric fields. *Journal of Geophysical Research: Space Physics*, *102*(A11), 24037–24046. https://doi.org/10.1029/97JA02165

Sheng, C., Y. Deng, C. Gabrielse, L. Lyons, Y. Nishimura, R. Heelis, Y. Chen (2021), Sensitivity of Upper Atmosphere to Different Characteristics of Flow Bursts in the Auroral Zone, *J. Geophys. Res.: Space Physics*, *126*, e2021JA029253

Tsurutani, B., Mannucci, A., Iijima, B., Abdu, M. A., Sobral, J. H. A., Gonzalez, W., Guarnieri, F., Tsuda, T., Saito, A., Yumoto, K., Fejer, B., Fuller-Rowell, T. J., Kozyra, J., Foster, J. C., Coster, A., & Vasyliunas, V. M. (2004). Global dayside ionospheric uplift and enhancement associated with interplanetary electric fields. *Journal of Geophysical Research: Space Physics*, *109*(A8). https://doi.org/10.1029/2003JA010342

Vierinen, J., Coster, A. J., Rideout, W. C., Erickson, P. J., & Norberg, J. (2016). Statistical framework for estimating GNSS bias. *Atmospheric Measurement Techniques*, *9*(3), 1303–1312. https://doi.org/10.5194/amt-9-1303-2016

Waters, C. L., Anderson, B. J., Green, D. L., Korth, H., Barnes, R. J., & Vanhamäki, H. (2020). Science Data Products for AMPERE. In M. W. Dunlop & H. Lühr (Eds.), Ionospheric Multi-Spacecraft Analysis Tools: Approaches for Deriving Ionospheric Parameters (pp. 141–165). Springer International Publishing. https://doi.org/10.1007/978-3-030-26732-2_7

Waters, C. L., Anderson, B. J., & Liou, K. (2001). Estimation of global field aligned currents using the iridium® System magnetometer data. Geophysical Research Letters, 28(11), 2165–2168. https://doi.org/10.1029/2000GL012725

Weimer, D. R. (2005). Improved ionospheric electrodynamic models and application to calculating Joule heating rates. Journal of Geophysical Research: Space Physics, 110(A5). https://doi.org/10.1029/2004JA010884

Zhang, S.-R., Erickson, P. J., Coster, A. J., Rideout, W., Vierinen, J., Jonah, O., & Goncharenko, L. P. (2019). Subauroral and Polar Traveling Ionospheric Disturbances During the 7–9 September 2017 Storms. *Space Weather*, *17*(12), 1748–1764. https://doi.org/10.1029/2019SW002325

Zhu, Q., Deng, Y., Maute, A., Kilcommons, L. M., Knipp, D. J., & Hairston, M. (2021). ASHLEY: A New Empirical Model for the High-Latitude Electron Precipitation and Electric Field. Space Weather, 19(5), e2020SW002671. https://doi.org/10.1029/2020SW002671

Zhu, Q., Deng, Y., Richmond, A., McGranaghan, R. M., & Maute, A. (2019). Impacts of Multiscale FACs on the Ionosphere-Thermosphere System: GITM Simulation. Journal of Geophysical Research: Space Physics, 124(5), 3532–3542. https://doi.org/10.1029/2018JA026082

Zhu, Q., Lu, G., Deng, Y. (2022). Low- and Mid-Latitude Ionospheric Response to the 2013 St. Patrick's Day Geomagnetic Storm in the American Sector:

Global Ionosphere Thermosphere Model Simulation. *Front. Astron. Space Sci.* 9:916739. doi: 10.3389/fspas.2022.916739

Run	Name	High-latitude potential	High-latitude electron precipitation
1	AMIE-driven	AMIE electric potential	AMIE electron precipitation
2	FAC-AMIE	Calculated using FAC	AMIE electron precipitation
3	FAC-ASHLEY	Calculated using FAC	ASHLEY-A
4	FAC-Robinson	Calculated using FAC	Derived from Robinson et al (2020)

Table 1. Summary of the simulations

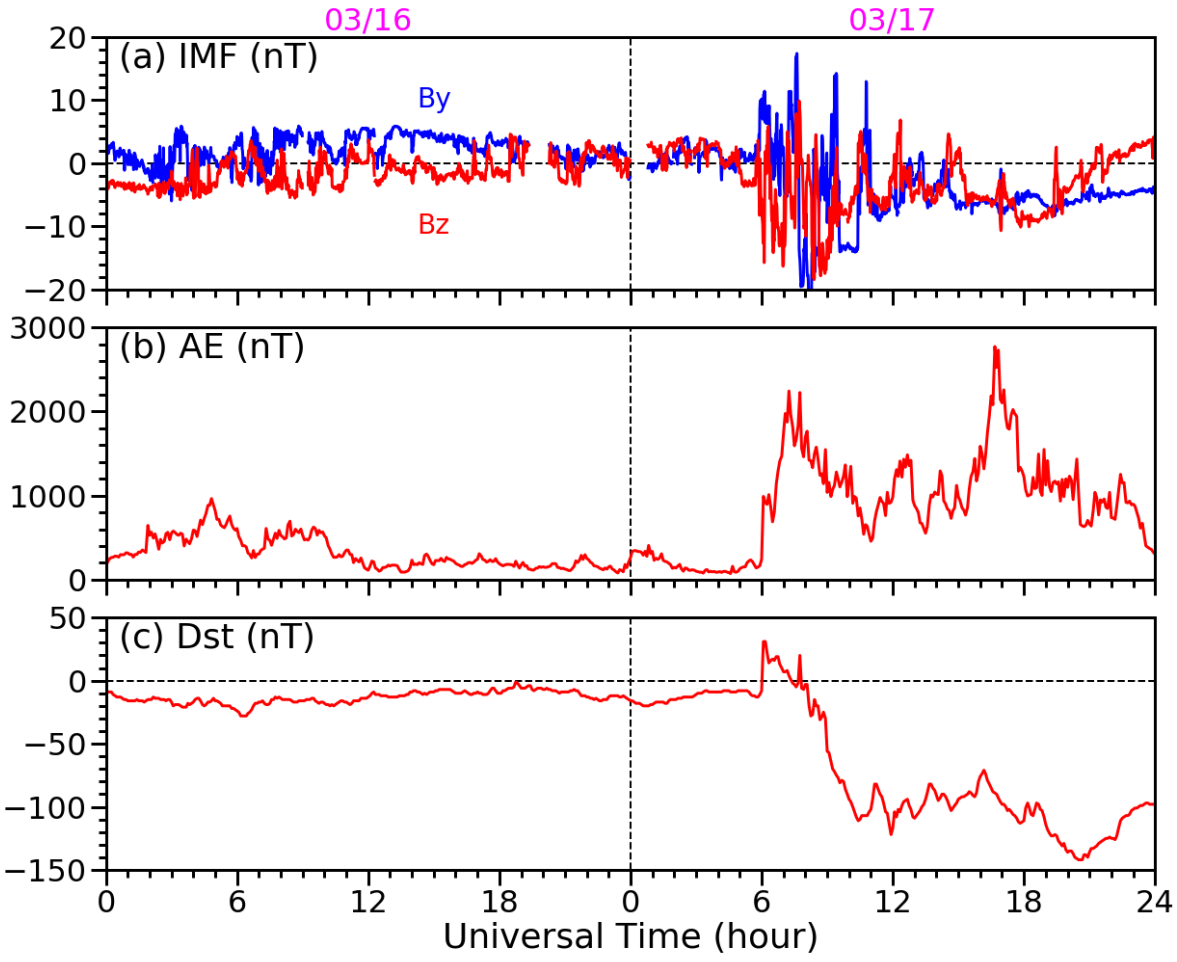

Figure 1. Evolutions of (a) IMF (blue: B_y; red: B_z), (b) AE and (c) Dst during the 2013 St Patrick's day geomagnetic storm. The parameters shown in the bottom two panels are from the Northern Hemisphere AMIE output.

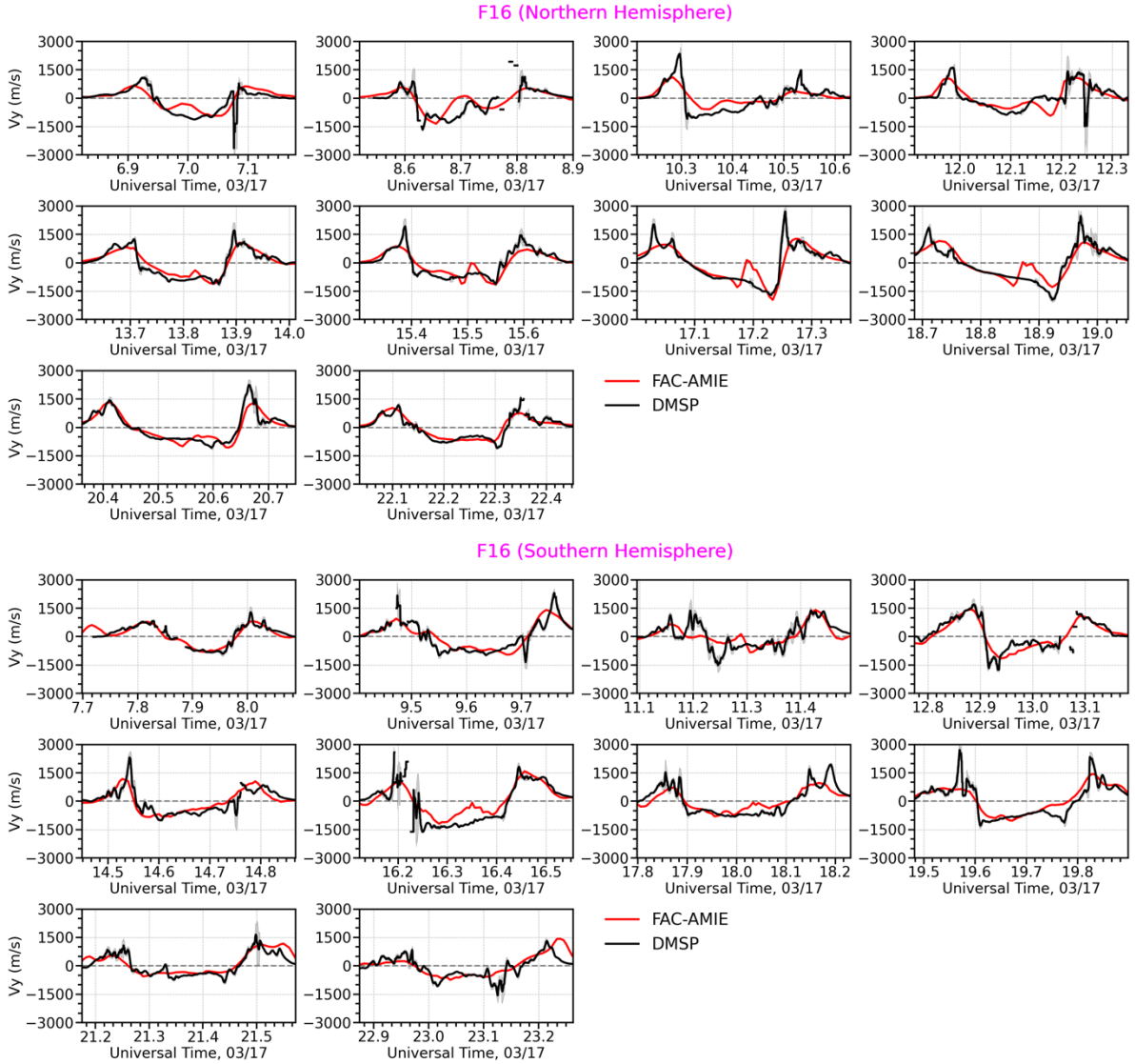

Figure 2. Comparisons of the cross-track ion drifts along the DMSP F16 polar crossings in the NH and SH. In each plot, black and red lines represent the DMSP measurement and FAC-AMIE simulation result, respectively.

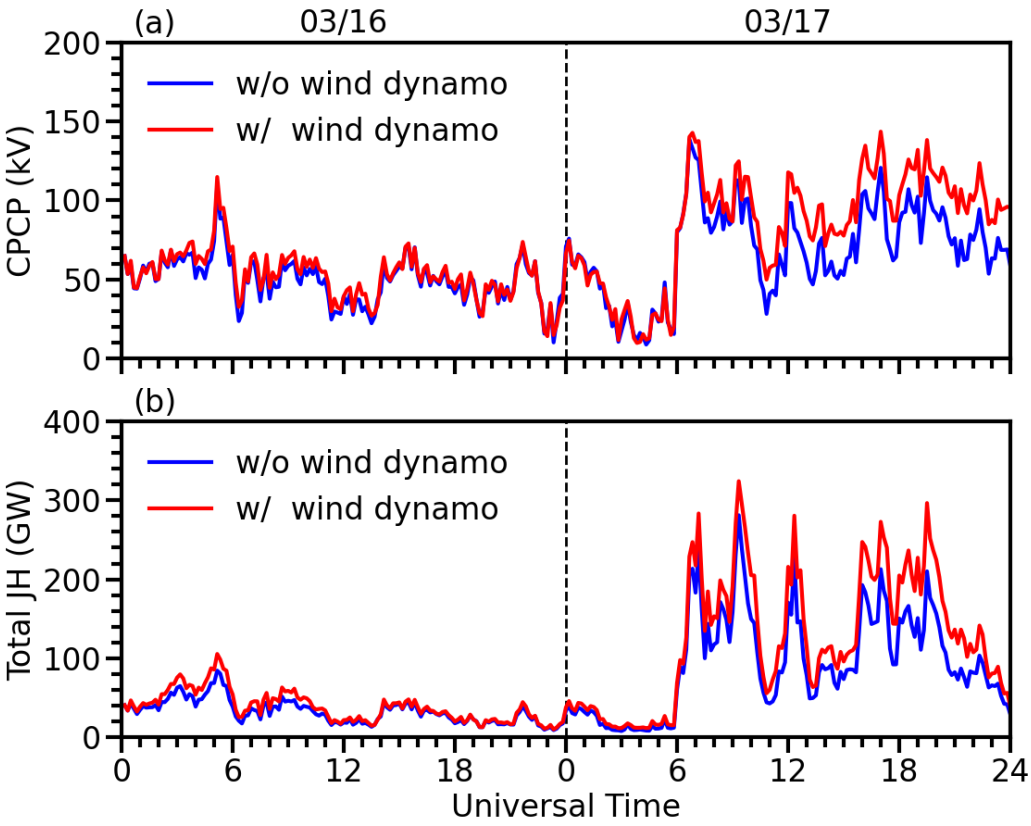

Figure 3. Comparisons of the cross-polar-cap potential and total Joule heating in the NH from two FAC-AMIE simulations. Red and blue lines represent the results from the FAC-AMIE simulations where the high-latitude wind dynamo is turned on and off, respectively.

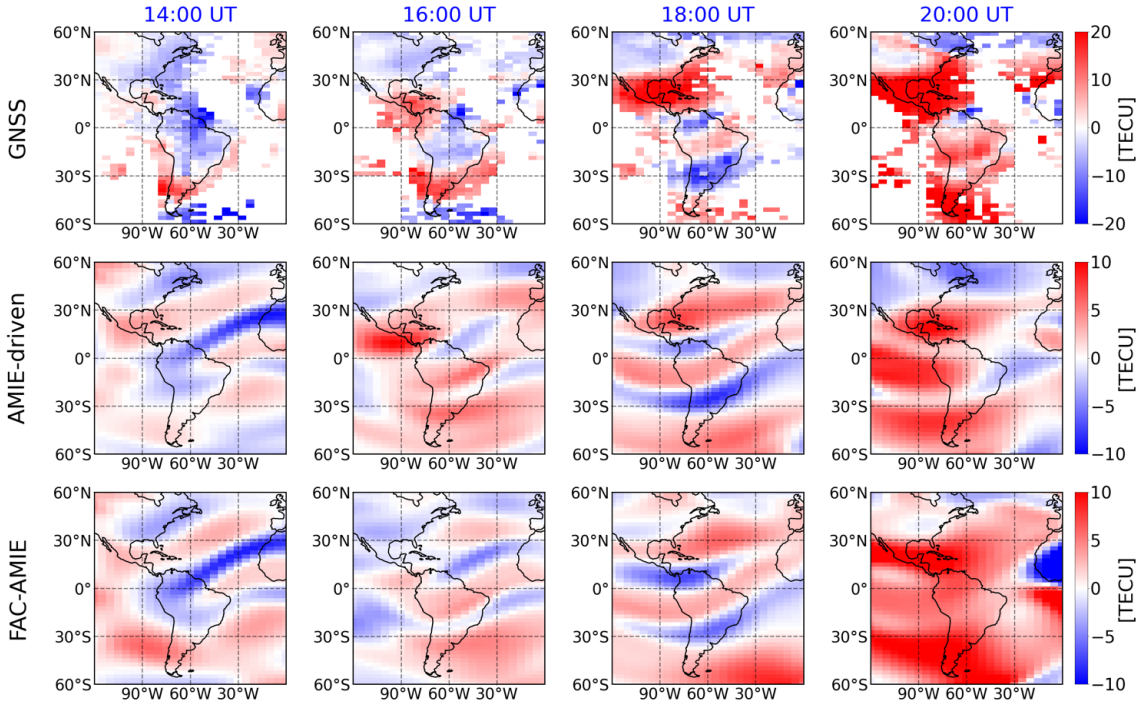

Figure 4. Comparisons of the storm-quiet differential TEC in the American sector at different UTs. At each UT, from top to bottom, the results correspond to those calculated from the observation, AMIE-driven and FAC-AMIE GITM simulation outputs, respectively. Note that the color scale ranges are smaller for those calculated from GITM simulation outputs.

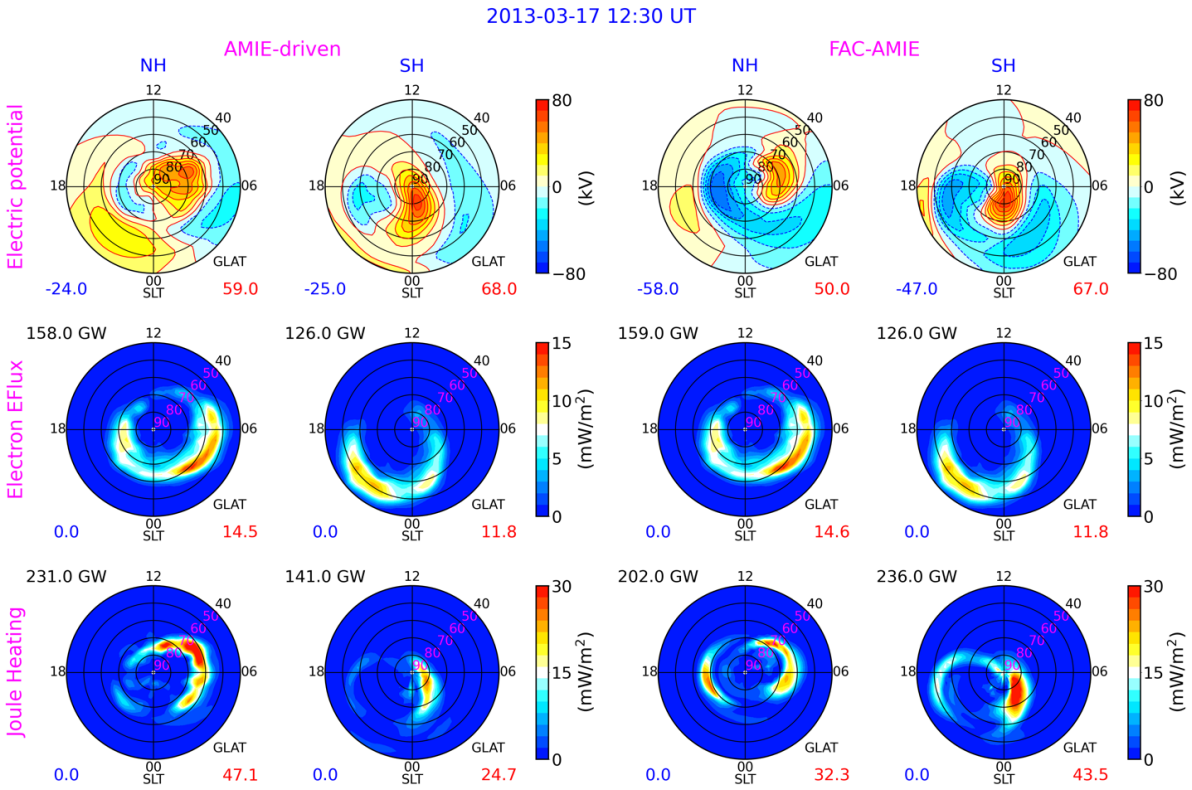

Figure 5. Distributions of the electric potential, total electron energy flux and height-integrated Joule heating from the AMIE-driven simulation (left two columns) and FAC-AMIE simulation (right two columns) at 12:30 UT on 03/17. The first and third rows correspond to outputs in the Northern Hemisphere while the second and fourth rows correspond to outputs in the Southern Hemisphere. For each plot, the minimum and maximum of the corresponding parameter are labelled at the bottom left and right of the plot, respectively. The value at the top left of each plot in the bottom two rows represents the hemispheric integrated value.

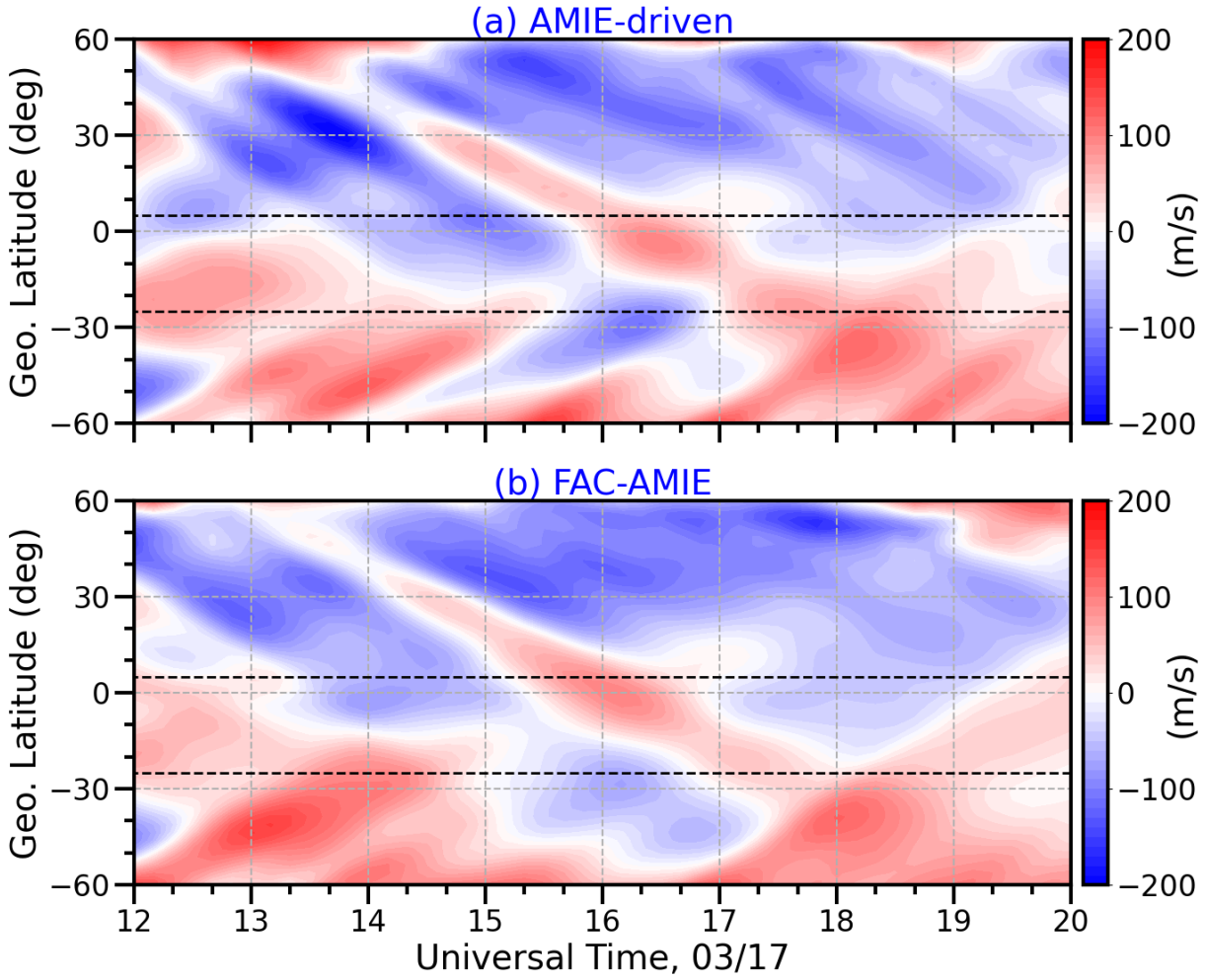

Figure 6. Comparisons of the storm-quiet differential meridional winds at 400 km and along 70°W as a function of UT and geographic latitudes between the (a) AMIE-driven and (b) FAC-AMIE simulations. The horizontal dashed lines in each plot denote 5°N and 25°S.

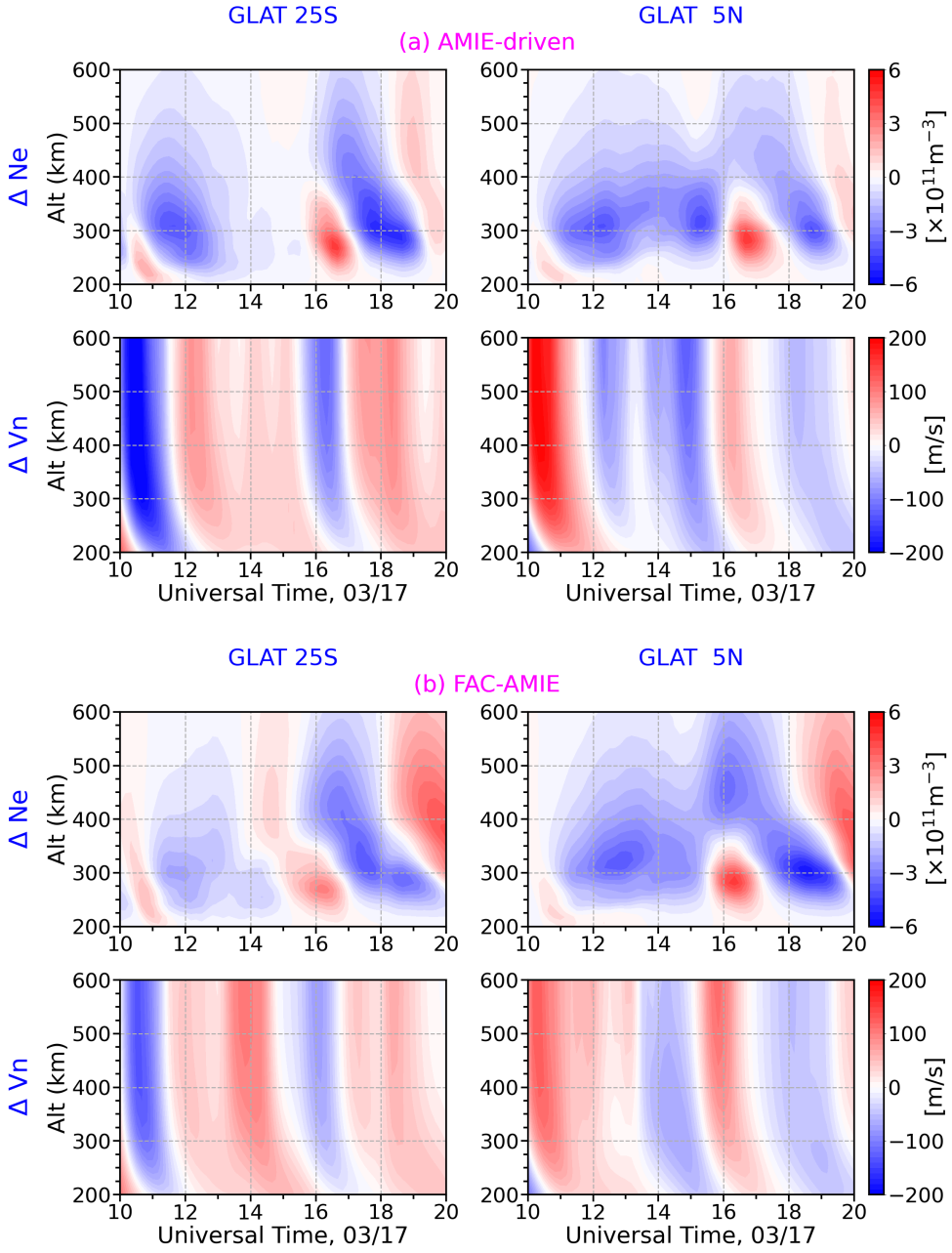

Figure 7. Storm-quiet differences of the electron density (Ne) and meridional wind (Vn) at 25°S and 5°N along 70°W from the (a) AMIE-driven and (b) FAC-

AMIE simulations. The parameter is shown as a function of UT and altitude. For the meridional wind, positive values indicate northward winds (poleward in the NH and equatorward in the SH).

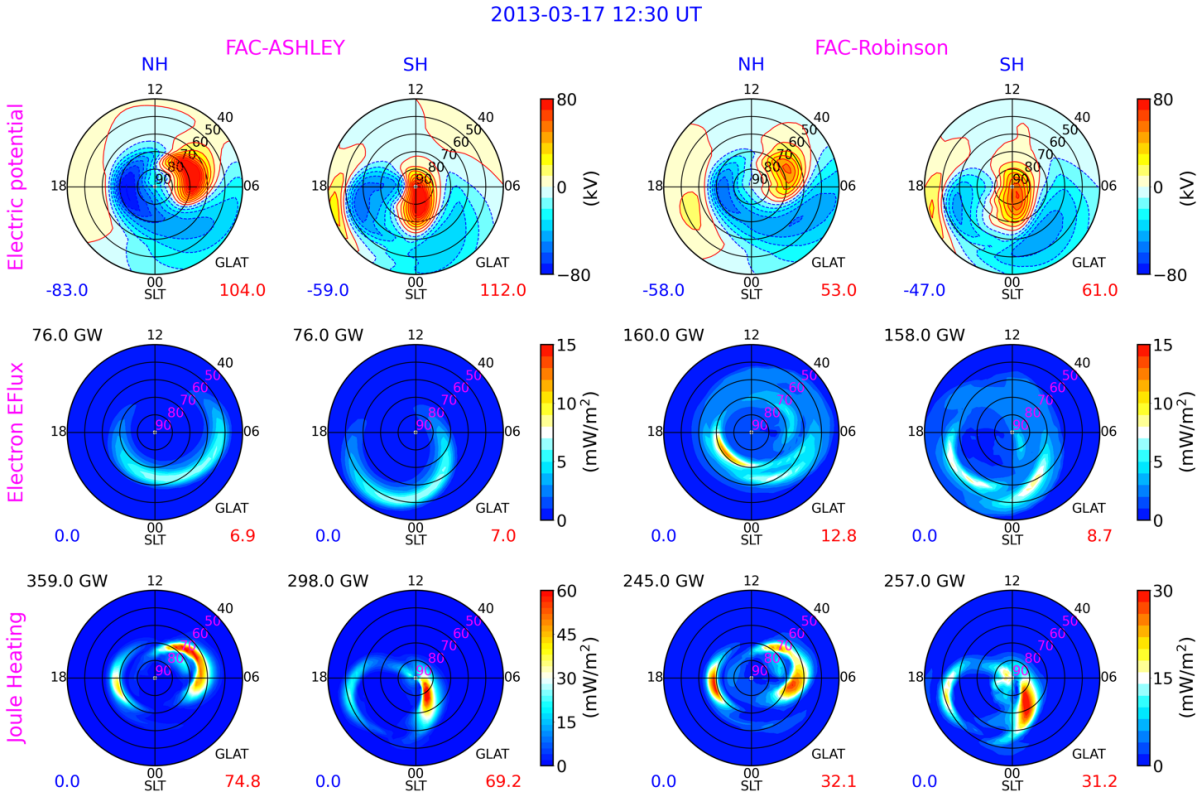

Figure 8. Same as Figure 5 but for the outputs from the FAC-ASHLEY simulation (left two columns) and FAC-Robinson simulation (right two columns). Note that the color scale for the height-integrated Joule heating from the FAC-ASHLEY simulation is twice as that for the height-integrated Joule heating from the FAC-Robinson simulation.

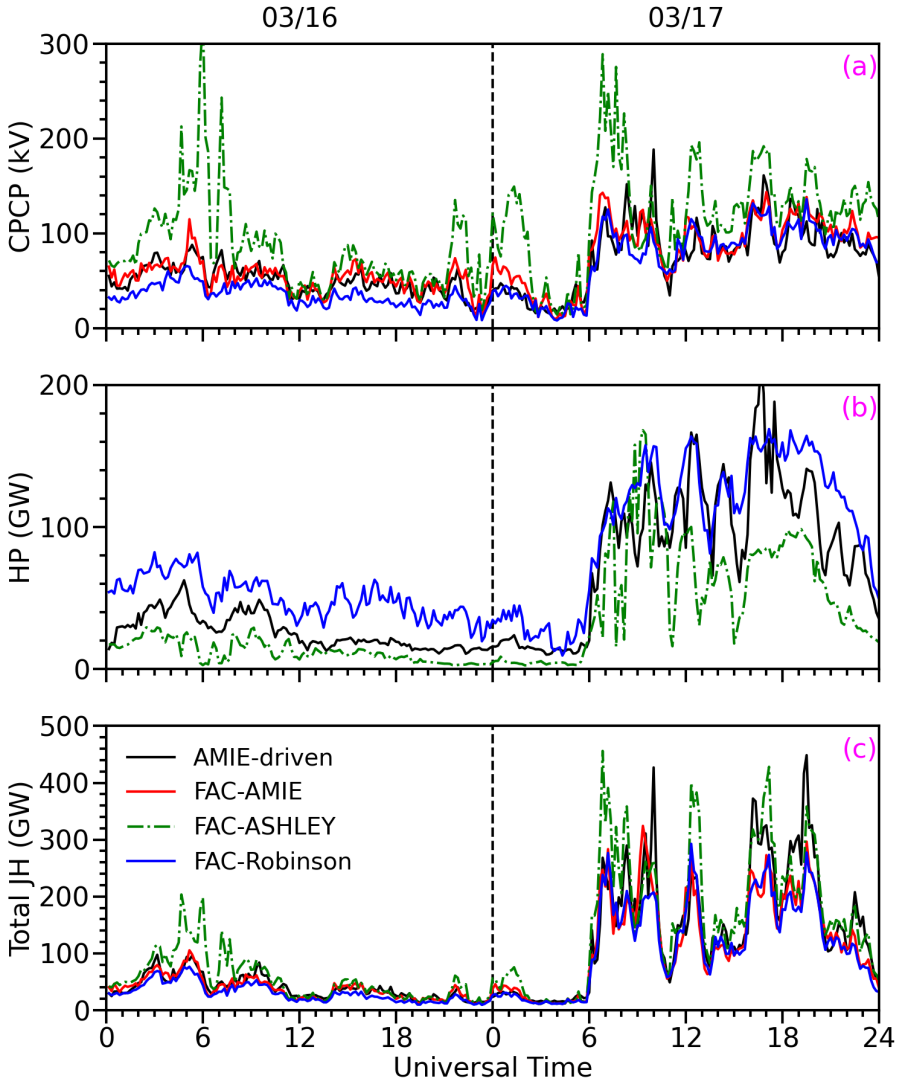

Figure 9. Comparisons of the (a) cross-polar-cap potential, (b) hemispheric power and (c) hemispheric-integrated Joule heating in the Northern Hemisphere. The outputs from the AMIE-driven, FAC-AMIE, FAC-ASHLEY and FAC-Robinson simulations are indicated by the black solid, red solid, green dashed and blue solid lines, respectively.